ARL-TR-8941 ● APR 2020

DEVCOM ARMY RESEARCH LABORATORY

Isotope Energy Release and Deposition Characteristics in Betavoltaic Materials

by Marc Litz, Randy Tompkins, Johnny Russo, Claude Pullen, Iain Kierzewski, Stephen Kelley, Mohamed Doumbia, Brenda Smith

NOTICES

Disclaimers

The findings in this report are not to be construed as an official Department of the Army position unless so designated by other authorized documents.

Citation of manufacturer's or trade names does not constitute an official endorsement or approval of the use thereof.

Destroy this report when it is no longer needed. Do not return it to the originator.

ARL-TR-8941 ● APR 2020

Isotope Energy Release and Deposition Characteristics in Betavoltaic Materials

Marc Litz, Randy Tompkins, Johnny Russo, Claude Pullen, and Mohamed Doumbia
Sensors and Electron Devices Directorate, CCDC Army Research Laboratory

Iain Kierzewski and Stephen Kelley
General Technical Services

Brenda Smith
Physical Sciences Directorate, Oak Ridge National Laboratory

REPORT DOCUMENTATION PAGE

Form Approved
OMB No. 0704-0188

1. REPORT DATE *(DD-MM-YYYY)*	2. REPORT TYPE	3. DATES COVERED (From - To)
April 2020	Technical Report	15 June 2019–15 February 2020

4. TITLE AND SUBTITLE
Isotope Energy Release and Deposition Characteristics in Betavoltaic Materials

5a. CONTRACT NUMBER

5b. GRANT NUMBER

5c. PROGRAM ELEMENT NUMBER

6. AUTHOR(S)
Marc Litz, Randy Tompkins, Johnny Russo, Claude Pullen, Iain Kierzewski, Stephen Kelley, Mohamed Doumbia, Brenda Smith

5d. PROJECT NUMBER

5e. TASK NUMBER

5f. WORK UNIT NUMBER

7. PERFORMING ORGANIZATION NAME(S) AND ADDRESS(ES)
CCDC Army Research Laboratory
ATTN: FCDD-RLS-CC
Aberdeen Proving Ground, MD 21001

8. PERFORMING ORGANIZATION REPORT NUMBER
ARL-TR-8941

9. SPONSORING/MONITORING AGENCY NAME(S) AND ADDRESS(ES)

10. SPONSOR/MONITOR'S ACRONYM(S)

11. SPONSOR/MONITOR'S REPORT NUMBER(S)

12. DISTRIBUTION/AVAILABILITY STATEMENT
Approved for public release; distribution is unlimited.

13. SUPPLEMENTARY NOTES

14. ABSTRACT
A Monte Carlo nuclear scattering code—Monte Carlo n-particle extended (MCNPX)—has been used to calculate electron energy losses in liquid-form radioisotope (RI) layers deposited on the surface of wide-bandgap semiconductor PIN junctions. The RI medium self-attenuation limits the RI layer thickness that is practical to deposit on the surface in order to achieve maximum electrical power output. The optimized RI layer thickness is defined here as the thickness that generates electrical power at 90% of the maximum energy transferrable to an underlying semiconductor layer. Liquid form isotope formats are evaluated using the optimal thickness approach as defined. It is found that for liquid form isotopes of 3 H, 63 Ni, 147 Pm, and 90 Sr, the optimal thicknesses are 2, 15, 50, and 250 μm thick, respectively. These results can vary in practice because of recrystallization rate and humidity uptake in the liquid form RI over time, but are useful for design of prototypes, basis for material comparison, and providing guidance for future experimental goals. This evaluation is expected to serve as a reference that enables predictions in future design of stacked volumetric power sources.

15. SUBJECT TERMS
wide-bandgap materials, betavoltaic, liquid-form radioisotopes, PIN diodes

16. SECURITY CLASSIFICATION OF:			17. LIMITATION OF ABSTRACT	18. NUMBER OF PAGES	19a. NAME OF RESPONSIBLE PERSON
a. REPORT	b. ABSTRACT	c. THIS PAGE			Marc S Litz
Unclassified	Unclassified	Unclassified	UU	36	19b. TELEPHONE NUMBER (Include area code) (301) 394-5556

Content

List of Figures

List of Tables

1. Introduction

Nuclear battery technology depends on atoms breaking apart, undergoing continuous decay processes. The five types of radioactive decay are alpha, beta, gamma, positron emission, and electron capture. The nuclei of atoms undergoing radioactive decay are unstable, but do follow the conservation laws (energy, momentum, charge, and nucleon number). The instability occurs in the interplay of the three nuclear forces: strong nuclear force (holding protons and neutrons together), the Coulomb force (repelling proton charged particles), and the weak nuclear force (acting inside individual nucleons). The weak force accounts for protons transforming into neutrons (and vice versa). In chemical reactions, the interactions are between electrons and atoms only. Chemical reaction rates increase by raising the temperature; however, nuclear reaction rates are unchanged under increasing temperatures.

The nuclear forces are powerful short-range forces within the nucleus. The energy of redistribution of protons and neutrons (~8 MeV binding energy) is much greater than the energy of redistributing atoms in their lattice associated with chemical energy transformations (~5 eV bond dissociation). The breakdown of an atom is 10^6 more energetic than the breakdown of a chemical bond. One of the merits of a nuclear battery is its high-energy density, which can be at least 10 times higher than that of hydrogen fuel cells and 1000 times higher than that of an electrochemical battery. Alphavoltaic and betavoltaic (BV) cells demonstrate high potential for use in low-power applications under a broad range of temperatures.

Thermionic and thermoelectric devices convert heat into electricity and are therefore heat engines which are limited by the Carnot efficiency. Direct energy conversion using BVs is not limited by Carnot efficiency; however, the efficiencies are typically still quite low (Krasnov et al. 2015, Theirrattanakul and Prelas 2017). These devices produce nW to mW with voltages ranging from 0.7 to 5 V depending on the semiconductor converting the kinetic energy of the decay product into electrical charge flow. However, BV devices can be compact and maintenance free because of the high-energy density and long half-life inherent in radioisotopes (RI).

The isotope high-energy density also makes these BV devices applicable to small implantable or micro-sensor devices. Electrical power from BV power sources is ideal for long-lived power applications that include space applications (Liu et al. 2014, Surampudi et al. 2017, Colozza et al. 2018) (especially beyond Saturn where solar flux is below threshold for photovoltaic conversion), harsh environments, or remotely located sensors (Calhoun et al. 2005) that are difficult to maintain or resupply with power. The high-energy density is a valuable characteristic in

lightweight micro-robotics, compact miniature sensors, or for powering critical-individual integrated circuit (IC) components in a larger system by applying a single layer isotope power source (Atallah et al. 2004, Helbling and Wood 2018).

Electrodeposition (ED) of ^{63}Ni on nickel foils is commonly performed for industrial applications as well as isotope power source fabrication for BV isotope power sources. The thickness of the ^{63}Ni layer is limited by self-absorption of the betas by the metal ED layer. ED layer thicknesses of 0.4–4 μm are common with maximum calculated and measured surface activity levels of 15 mCi/cm^2 reported (Belghachi et al. n.d., Wu et al. 2011, Gui et al. 2016, Uhm et al. 2016, Alam et al. 2017, Krasnov et al. 2019, Pustovalov et al. 2007). The approach of embedding the isotope in a liquid medium of lower mass density compared to metallic mass densities typical of ED achieves two goals. First, a thicker isotope layer can be deposited before self-shielding is reached. Second, uniform deposition can be achieved on (and within) 3-D structured energy converter (EC) compared to ED. This characteristic enables thicker layers and higher effective surface activity to be reached before self-attenuation overcomes efficacy of additional isotope layer thickness. In this report, we evaluate the use of liquid form RI. The isotopes of ^{3}H, ^{63}Ni, ^{35}S, ^{147}Pm, and ^{90}Sr have been modeled. The liquid forms modeled are shown in Table 1.

Table 1 Table of liquid form isotopes of interest and practical characteristics

RI	Liquid format	Crystallization density (g/cc)	Purity	Thickness (μm)	Ep[a] (keV)	Eavg[a] (keV)	Tau$_{1/2}$[a] (yr)	Dose[b] at 30 cm (μREM/h/mCi)	Theoretical/Practical Specific (Ci/g)	Activity[c]
^{3}H	^{3}H-urea	0.5	95%	4	18.59	5.68	12.32	0	9640	25
^{63}Ni	$^{63}NiCl_2$	1.5	95%	15	66.95	17.4	101.2	0	57	15
^{147}Pm	$^{147}PmCl_3$	1.55	30%	50	224.6	61.93	2.62	2.48(ɤ)	20000	74
^{35}S	$^{35}S(NH_4)_2$	0.997	99%	50	167.3	48.7	0.238	0	42840	0.006
^{90}Sr	$^{90}Sr(NO_3)_2$	0.99	95%	250	546	195	28.8	5513 (β)	140	77
^{90}Y	(from ^{90}Sr)	…	…	…	2280	933	0.007	…	…	…

[a] Decay energy from NuDat 2.8. National Nuclear Data Center; n.d. [accessed 2020]. https://www.nndc.bnl.gov/nudat2/.
[b] Delacroix D. Radionuclide and radiation protection data handbook. Nuclear Technology Publishing; 2002.
[c] Reynolds SA. Theoretical and practical specific activities and other properties of common radionuclides. ORNL; 1973 Mar. Report no.: ORNL-TM-4167.

With the rise in capability to fabricate 3-D structures comes the opportunity to increase the coupling between isotope and EC. Three-dimensional EC structures have been fabricated in Si (Duggirala et al. 2007, Miley et al. 2011, Krasnov et al. 2017) and diamond (Bormashov et al. 2018). Uniform ED over nonplanar, 3-D textured surfaces is difficult to achieve. Low-density liquid-format isotope offer the possibility to fill the gap spacing between mesas in 3-D structured BV devices. Deposition of liquids can be made scalable for manufacturing processes. By filling

in the gaps on 3-D structures with liquid-form isotope, an increase in the effective surface activity applied to the energy conversion device can be achieved.

In the following simulations, the full spectral shape and source isotropic emission are included in the calculation. It has been shown that average values of the emission spectrum are insufficient to accurately characterize the depth profile of RI energy deposited in the EC (Litz 2014, Alam et al. 2017). The spectra of five radioisotopes useful in applications are shown in Fig. 1 (Cross et al. 1983). The isotope half-lives vary from 0.17–99 years. The isotope endpoint energies vary from 0.018–2.2 MeV, detailed in Table 1. The specific activity varies from 57–550 k Ci/g (Reynolds 1973).

The modeling was performed using the Monte Carlo neutron-particle extended (MCNPX) nuclear scattering code (Pelowitz 2011). MCNPX is a general-purpose Monte Carlo code that can be used to model neutron, photon, and electron (or coupled) transport. The transport code can track 32 types of particles. The extensive set of libraries contained within the code includes cross-sectional data and is able to simulate the transportation of these particles with energy from 1 keV to 100 MeV in materials. The MCNPX code-sets are used for design of spallation targets, design and development of radiography and imaging technologies, nuclear materials detection, accelerator shielding, and dose/energy deposition in materials for medical therapies.

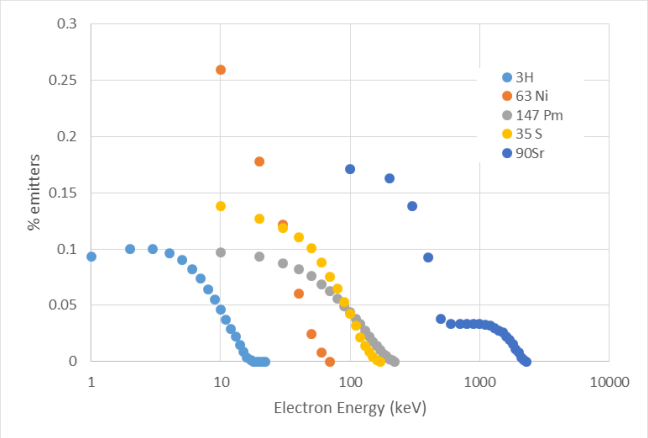

Fig. 1 The beta emission spectra for five available isotopes are shown on a log plot

2. Approach and Numerical Calculations

A planar rectangular layer of isotope is simulated on top of a larger planar rectangular EC. The physical geometry modeled is similar in all simulations, and shown in Fig. 2. The EC wide-bandgap (WBG) semiconductor (SC) layer is 60 × 60 μm^2 area. The EC thickness is typically 100 µm but increases to 3 mm

when applying ^{147}Pm and ^{90}Sr. The EC layer thickness is modified to ensure that all energy is accounted for in simulation volume and that energy conservation is verified, ensuring that all beta energy is captured and dissipated in the simulation configuration volume.

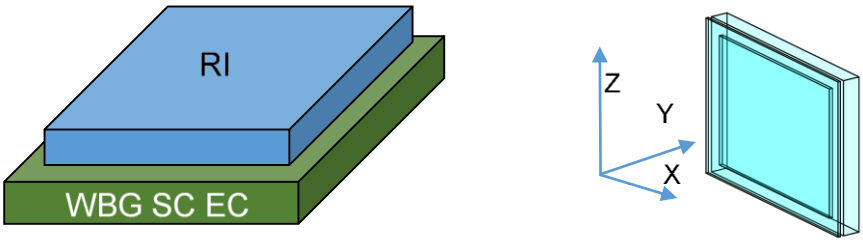

Fig. 2 a) The generalized geometry for the parametric study of RI thickness and range of energy deposition in EC is shown. b) The axis coordinates used in the simulation are added.

The first parameter investigated is the RI layer thickness. We begin with a 1-µm-thick layer and increase the RI layer thickness. When only 10% of the energy content within the RI layer is released, the RI layer thickness has become too thick to be practical or economical (cost of isotope). The energy entering the EC layer is calculated for each thickness of RI layer. The energy entering and deposited into the EC saturates at a RI thickness proportional to the range of the emitted betas in the RI layer material volume. (The self-shielding thickness of the RI medium can be measured by this method.) Both energy released by the RI layer and energy deposited in the EC layer are compared in Fig. 3. As the RI layer thickness increases, the monotonic-increasing energy released in the RI layer is shown (in blue) in Fig. 3. The saturation of energy (per second) deposited into the EC layer (in red) is compared to the energy content in the RI layer for a ^{63}Ni RI layer and a silicon carbide (SiC) EC. No more than 22 nJ/s can be deposited into the EC from a 50 × 50 µm^2 RI layer area. The energy deposited and stored in the source layer (50 × 50 × 20 µm^3) of density 1.5 g/cc, with a ^{63}Ni specific energy of 15 Ci/g (see Table 1) is approximately 170 nJ and the energy deposited into the SiC EC is approximately 22 nJ.

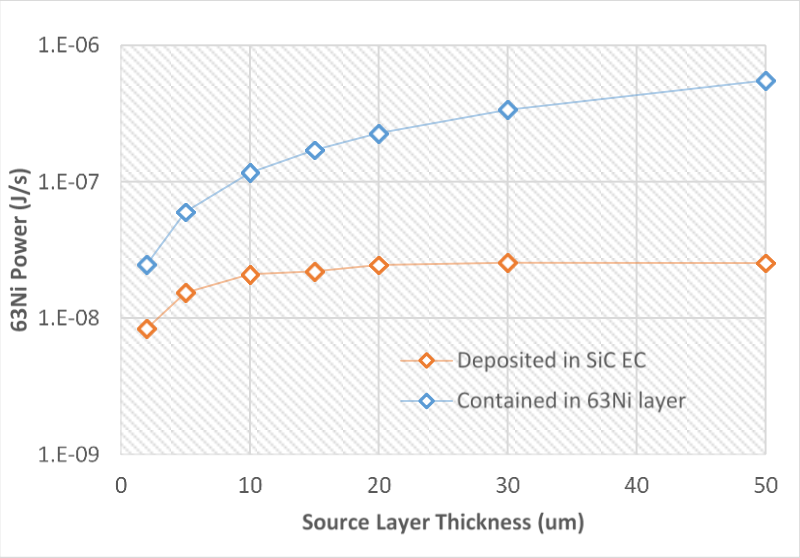

Fig. 3 The energy emitted by the nuclei within the ^{63}Ni layer continues to increase with layer thickness; however, the energy deposited into the energy-converting layer underneath is limited by self-attenuation

The example used here is $^{63}NiCl_2$ layer deposited on SiC. The beta spectrum emitted from the ^{63}Ni is shown in Fig. 4. The ^{63}Ni atom decays with a half-life of 101.2 years and has a maximum beta energy of 66.95 keV and an average beta energy of 17.43 keV. The beta spectrum for ^{63}Ni (Fig. 4) shows that 12 decays out of 100 have an energy between 12.5 and 17.5 keV, and 10 decays have an energy between 17.5 and 22.5 keV.

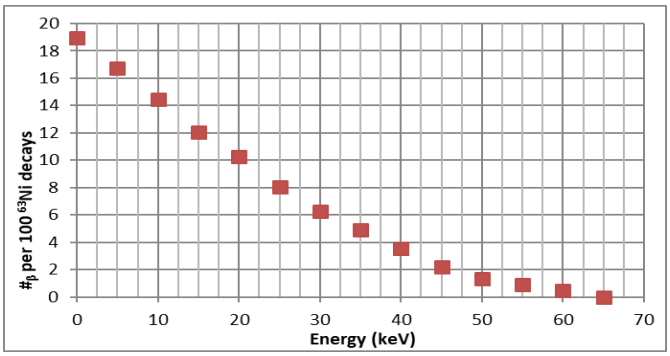

Fig. 4 The spectrum of ^{63}Ni beta emissions is sourced within the RI layer

The energy deposited by the RI into the RI layer (between 0–2 µm) and the SiC EC region (2–20 µm) is shown in Fig. 5a. The contour plot of energy deposition in units of MeV/g quantifies the energy deposition for ^{63}Ni in SiC EC. The ^{63}Ni energy deposition within the 0–2 µm RI layer decreases as you move out from the 1-µm centerline, visible as parabola between 0–2 µm in Fig. 5b. The higher energy betas in the spectrum penetrate further into the SiC EC. The energy deposition depth

profile is calculated and shown in Fig. 5b. The discontinuity of energy density (MeV/g) at the boundary of the RI layer and EC region appears because the material density changes. The mass density of RI layer composed of $^{63}NiCl_2$ is 1.5 g/cc and the mass density of the SiC EC is 3.2 g/cc.

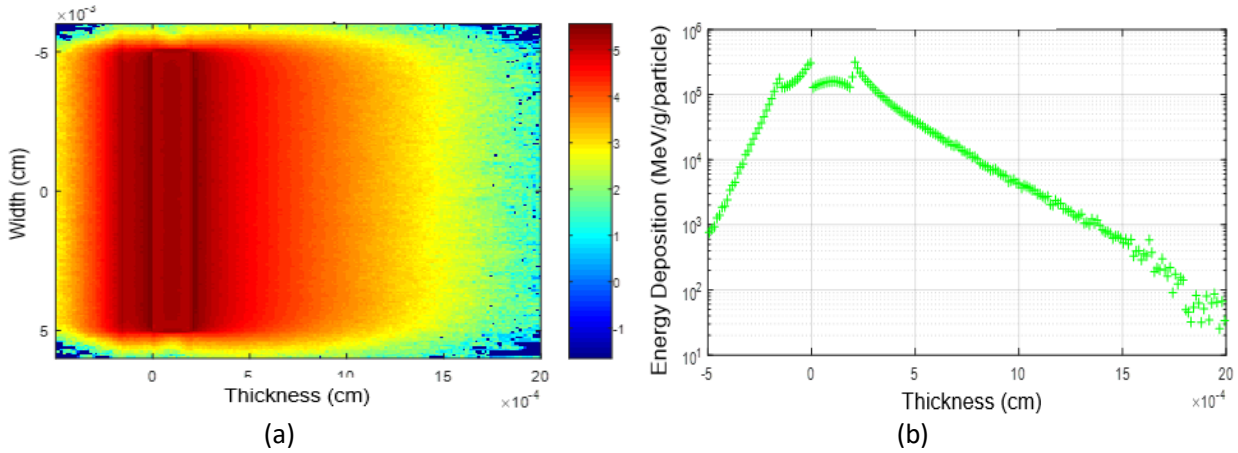

Fig. 5 a) The contour plot of energy deposited (MeV/g) through 20-µm-thick SiC EC is imaged. b) The energy deposition profile shows the reduced energy deposited by a factor of 100 within 10 µm of SiC.

The energy deposited in the SiC is maximum (3×10^5 MeV/g) in the region adjacent to the isotope layer, as shown in Fig. 5b at the position of 2 µm. The energy deposited by the ^{63}Ni layer falls to 1% of an approximate maximum of 12 µm into the SiC layer. The energy deposited after 3.5 µm (at the location of 5.5 µm in Fig. 5b) is 2×10^4 MeV/g.

The range at which 90% of the integrated energy is deposited into the energy converter is shown in Fig. 6. The energy saturates as the RI layer increases and self-shielding overcomes additional isotope. There is a tradeoff of the cost of adding more isotope with the return on energy deposited into the EC. The depth for 90% energy deposition in the SiC EC is always 4.5 µm when using ^{63}Ni. The tradeoff appears between efficiency (P_{elec}/P_{nuc}) and maximum power achievable. The most efficient use of RI layer, while mathematically 0, is more realistically 1 µm thickness, because minimal self-shielding and energy absorption of RI medium will occur. Therefore, maximum energy transfer will occur with minimum RI layer thickness. However, maximum power output per cm^2 is achieved at RI layer thickness such that energy deposition into EC layer no longer increases, and in fact saturates, as shown in Fig. 6 for $^{63}NiCl_2$ RI deposited on SiC EC. Integrating the energy deposition profile in the EC over the depth into the EC shows the saturated value of energy deposition is reached after 4.5 µm. The RI layer thickness that transfers 90% of maximum transferable energy from RI to EC is catalogued in

column 5 of Table 1. The thickness of 15 µm $^{63}NiCl_2$ RI layer is calculated to transfer 90% of the maximum transferrable energy into the SiC EC. A complete accounting of integrated energy deposition into selected WBG EC from available isotopes is plotted and tabulated in Appendix C.

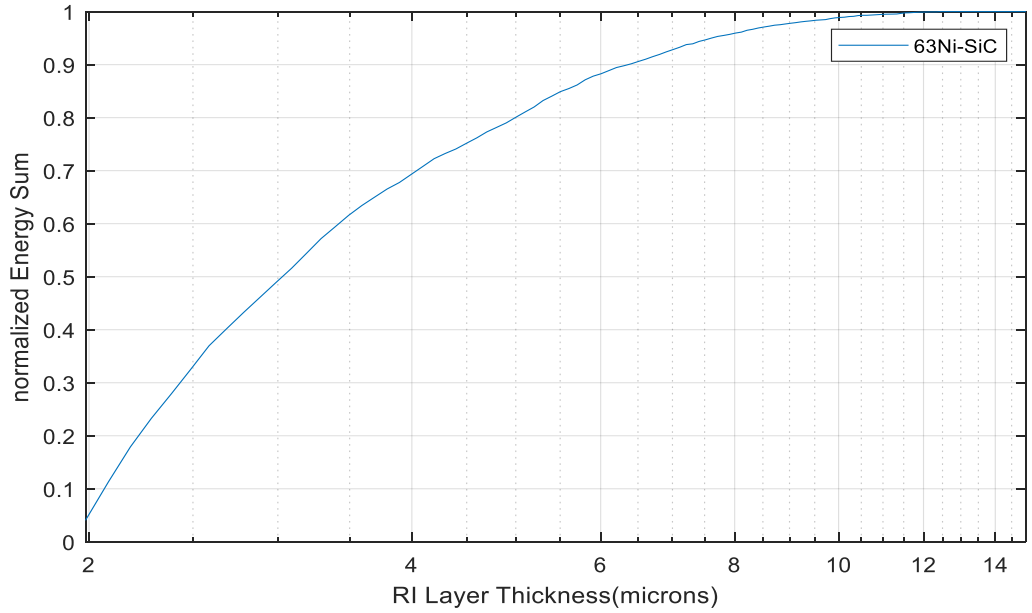

Fig. 6 The energy deposited into the SiC EC is integrated along the path (depth) showing that 90% of the energy is deposited in 4.5 µm of SiC, where the SiC layer starts at 2 µm

3. Results

A parametric study of RI thickness has been performed (for the radioisotopes of ^{3}H, ^{63}Ni, ^{35}S, ^{147}Pm, and ^{90}Sr) with the goal of calculating the energy transferred into the EC as a function of RI thickness, in Section 3.1. This analysis has been carried out using ^{3}H, ^{63}Ni, ^{147}Pm, ^{35}S, and ^{90}Sr using the beta spectra shown in Fig. 1. A second parametric study varying EC material shows the energy deposition range for the list of isotopes into the WBG materials of SiC, gallium nitride (GaN), and diamond in Section 3.2.

3.1 Self-Attenuation/Energy Deposition in Liquid Form RI (Self-Attenuation)

The approach used in calculating the RI layer thickness is described in Section 2. The results for the RI layer thickness that deposits 90% of the transferable energy into EC is shown in column 5 of Table 1.

The liquid form isotope utilized are mixed with a 5:1 ethanol-methanol solution during deposition in experiments. The methanol:ethanol mixture evaporates

leaving a crystalized remainder form of the isotopes listed. The crystalized remainder has been measured to have a mass density approximately one-third the mass density of the solid. The purity of the isotope is dependent on production method (i.e., reactor, linac), separation radiochemistry utilized, neutron flux, and neutron reaction cross section. The β-spectrum of ^{63}Ni is shown in Fig. 4. The endpoint energy is 66.95 keV with an average spectrum energy of 17.4 keV and half-life of 101.2 years. These values are tabulated for all isotopes of interest. The dose tabulated reflects the level of measureable radiation at a distance of 1 ft from a point source. All beta sources (with the exception of ^{90}Sr) are significantly attenuated. Bremsstrahlung radiation from ^{147}Pm is the major source of dose contribution. ^{90}Y betas (daughter of ^{90}Sr) do reach out to 60 ft contributing to the largest measureable dose at 1 ft in the list of isotopes. Practical specific activities are based upon evaluated neutron cross sections and fission yields, as well as analytical data. Flux values were those typical of the ORNL High Flux Isotope Reactor (HFIR), approximately 2×10^{15} n/s for a week or less, and approximately 8×10^{14} n/s for longer irradiations.

Thickness is calculated based on 90% of the maximum saturable energy that can be deposited in the energy converter. As the thickness of the RI layer increases, a limit is reached at which no more energy will be transmitted to the surface because of self-shielding. The thickness of the RI layer when the energy transferred is 90% of the maximum is calculated in column 5 of Table 1.

Liquid form radioisotopes are commonly used in biomedical research as tracers that are included in the bloodstream (Osso et al. 2009, Maloth et al. 2014, Weaver et al. 2016). The compounds are available because they can be readily synthesized. We have identified several radioisotope compounds that are commercially available. We have calculated optimal values of isotope layer thickness based on the compound density and specific activity. The remainder density has been empirically determined experimentally to be approximately one-third the crystalline form.

The calculated values of RI layer thickness are shown for all radioisotopes in Appendix A. The method for the calculation is described in Section 2 and Fig. 3 of this report.

3.2 Energy Deposition of RI in WBG Semiconductor Energy Converter

The range of penetration of energetic electrons in semiconductors is primarily dependent on the energy of the incoming electron, the elemental composition of the semiconductor energy converter, and the density of the semiconductor. The

penetration depth and resulting energy deposition in materials has been investigated in a variety of semiconductors including SiC, GaN, zinc sulfide (ZnS), and diamond. It is useful to compare the distance/range over which energy deposition from isotope spectra occur. The energy deposition range (and related electron penetration range) for isotopes of interest into SiC is shown in Fig. 7. The depth for which 90% of the total energy deposition occurs in SiC is shown in column two of Table 2, matching the graphical energy deposition of Fig. 7.

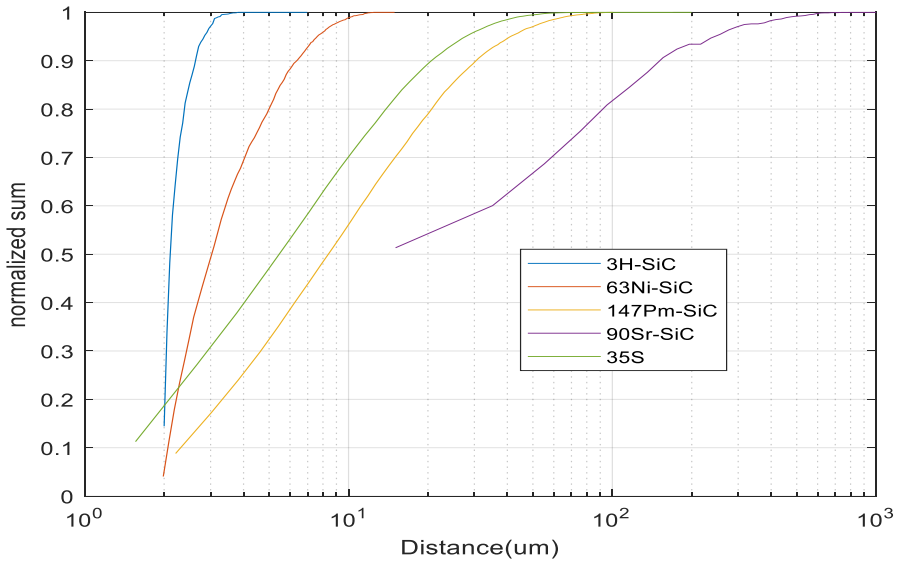

Fig. 7 The distance in SiC over which normalized total energy from five isotopes is deposited is calculated. The liquid RI layer thickness is 2 µm for all examples, followed by 1-mm-thick SiC energy converter.

The values for aluminum gallium nitride (AlGaN) are similar to that of GaN. The depth value for ^{147}Pm in SiC has been experimentally verified.

Table 2 Energy from isotope layer deposited on EC materials creates exponential depth profile. The depth (µm) in which 90% of the energy is deposited is shown.

	SiC	GaN	Diamond	ZnS	^{3}H-urea	$^{63}NiCl_2$	$^{147}PmCl_3$	$^{35}S(NH_4)_2$	$^{90}Sr(NOH_3)$
^{3}H	0.62	0.23	0.42	1.4	3.4		…	…	…
^{63}Ni	4.4	2.2	3.3	8	…	11.5	…	…	…
^{147}Pm	28.4	14.8	23	40	…	…	42	…	…
^{35}S	18.5	10	15	36	…	…	…	45	…
^{90}Sr	149	130	69.5	231	…	…	…	…	198
g/cc	3.2	6.15	4.5	1.5	.5	1.05	1.55	.99	.99
BG	Indirect	Direct	Indirect	Direct	…	…	…	…	…

4. Conclusions

A parametric study of RI layer thickness was performed. Both the most efficient RI layer thickness and the RI layer thickness that produced maximum power output has been calculated. The most efficient RI layer thickness is defined here as the RI thickness that produces the largest ratio of electron-scattered energy deposited in EC/nuclear decay energy contained within the RI layer deposited on EC. In a world where energy efficiency is the highest priority, then the RI layer thickness of ^{3}H, ^{63}Ni, ^{147}Pm, and ^{90}Sr are 2, 5, 20, and 100 µm, respectively. However, the RI thickness that maximizes energy output per cm^2 of surface area is tabulated in Table 3. As the RI layer increases, self-shielding overcomes addition of isotope. When 90% of the maximum energy deposited into the EC is reached, as the RI layer increases, the nuclear power converted to electrical and the cost of isotopes is prohibitive/useless/not valuable. The RI layer thickness at which 90% of the maximum saturable energy transferred from isotope to EC is tabulated in column two along with the volume of isotope deposited per square centimeter on the EC, the density of the isotope, and the specific activity. From these material characteristics the isotope activity per square centimeter for a betavoltaic can be estimated. The cost per cm^2 of RI on small quantity purchases from commercial vendors can be large, making accurate cost estimate difficult. In a real demonstration, the RI costs would likely be reduced because of volume cost savings in a large quantity production and likely reduction in cost from use of RI in nuclear waste stream. The values tabulated are generated from liquid form isotopes of tritiated-urea (1.1 g/cc), $^{63}NiCl_2$ (1.55 g/cc), $^{147}PmCl_3$ (0.9 g/cc), $^{90}Sr(NO_3)_2$ (0.99 g/cc). The density values are approximately one-third the values for the solid form, resulting from experimental observations to-date.

Table 3 Isotope activity that can be deposited on planar energy converters per square centimeter is estimated from simulation results and specific activity (ORNL NIDC production values)

Isotope	90% saturated		RI	RI	Activity per cm^2 mCi
	RI layer thickness µm	RI vol/cm^2 cc	Liquid density g/cc	Specific activity Ci/g	
3H-urea	2	0.0002	1.1	1000	220
NiCl2	15	0.0015	1.5	13	29
PmCl3	50	0.005	0.9	74	165
Sr(No3)2	250	0.025	0.99	25	619

The values estimated for activity per cm2 are greater than estimates and availability using electrodeposition techniques. These calculations are for planar betavoltaic devices. When used with textured structures of EC, the conformal deposition of

liquid form isotope is expected to provide a higher output power per square centimeter.

Future efforts will include investigation of degradation of EC as a function of RI energy profiles. Degradation of materials from incident electron energy is dependent on fluence of RI source semiconductor compound characteristics, which include lattice constant, bond strength, displacement energy, and atomic number (Wort and Balmer 2008, Spencer and Alam 2019). A figure of merit based on semiconductor bandgap (BG)/lattice constant (LC) would suggest that AlGaN and diamond should be radiation tolerant (see Appendix B). AlGaN and diamond semiconductors are less developed that SiC and GaN at present.

The calculation of isotope penetration into energy conversion materials has become an important tool in optimizing devices. The results enable matched pairs of isotope and energy converters to be developed. Increasing the energy density of these devices by stacking layers into arrays of devices (Bormashov et al. 2018, Russo et al. 2019) adds another dimension of value to the development of power sources and the efficient use of isotope energy matching to energy converter geometries.

5. References

Alam TR, Pierson MA, Prelas MA. Beta particle transport and its impact on betavoltaic battery modeling. Applied Radiation and Isotopes. 2017;130:80–89.

Atallah MJ, Bryant ED, Stytz MR. A survey of anti-tamper technologies. CrossTalk: The Journal of Defense Software Engineering. 2004;17(11).

Belghachi A, Bozkurt K, Moughli H, Ozdemir O, Amiri B, ATalhi. A model for Ni-63 source for betavoltaic application. arXiv:1903.09098v1 (physics.app-ph).

Bormashov VS, Troschieva SY, Tarelkina SA, Volkova AP, Teteruka DV, Golovanova AV, Kuznetsova MS, Kornilova NV, Terentieva SA, Blank VD. High power density nuclear battery prototype based on diamond Schottky diodes. Diamond and Related Materials. 2018;84:41–47.

Colozza AJ, Cataldo RL. Low power radioisotope conversion technology and performance summary. Washington (DC): National Aeronautics and Space Administration; 2018. Report No.: NASA/TM—2018-219940.

Calhoun BH, Daly DC, Verma N, Finchelstein DF, Wentzloff DD, Wang A, Cho SH, Chandrakasan AP. Design considerations for ultra-low energy wireless microsensor nodes. IEEE Trans Comput. 2005;54(6):727–740.

Cross WG, Ing H, Freedman N. A short atlas of beta-ray spectra. Phys Med Biol. 1983;28(11):1251–1260.

Duggirala R, Tin S, Lal A. 3-D silicon betavoltaics microfabricated using a self-aligned process for 5mW/cc average, 5-year lifetime microbatteries. Proceedings of Transducers 2007 – International Solid-State Sensors, Actuators and Microsystems Conference; 2007 June; Lyon, France.

Gui G, Zhang K, Blanchard JP, Ma Z. Prediction of 4H–SiC betavoltaic microbattery characteristics based on practical Ni-63 sources. Applied Radiation and Isotopes. 2016;107:272–277.

Helbling EF, Wood RJ. A review of propulsion, power, and control architectures for insect-scale flapping-wing vehicles. Applied Mechanics Reviews, ASME. 2018;70.

Krasnov AA, Legotin SA, Omel'chenko YK, Didenko SI, Murashev VN, Rabinovich OI, Yurchuk SY, Yaromsky VP, Popkova AV. Optimization of energy conversion efficiency betavoltaic element based on silicon. Journal of Nano- and Electronic Physics. 2015;7(4):04004.

Krasnov AA, Legotin S, Kuzmina K, Ershova N, Rogozev B. A nuclear battery based on silicon p-i-n structures with electroplating 63Ni layer. Nuclear Engineering and Technology. 2019;51(8):1978–1982.

Krasnov AA, Starkov VV, Legotin SA, Rabinovich OI, Didenko SI, Murashev VN, Cheverikin VV, Yakimov EB, Fedulova NA, Rogozev BI, Laryushkin AS. Development of betavoltaic cell technology production based on microchannel silicon and its electrical parameters evaluation. Applied Radiation and Isotopes. 2017;121:71–75.

Litz M. Monte Carlo evaluation of tritium beta spectrum energy deposition in gallium nitride direct energy conversion devices. Aberdeen Proving Ground (MD): Army Research Laboratory (US); 2014 Sep. Report No.: ARL-TR-7082.

Liu Y-P, Tang X-B, Xu Z-H, Hong L. Geng C-R, Chen D. Energy deposition, parameter optimization, and performance analysis of space radiation voltaic batteries. Nuclear Science and Techniques. 2014;25:S010402.

Maloth KN, Velpula N, Ugrappa S, Kodangal S. Radioisotopes: an overview. Int J Case Rep Images. 2014;5(9):604–609.

Miley GH, Lou N, Nanopore A. Multilayer isotope battery using radioisotopes from nuclear wastes. 9th Annual International Energy Conversion Engineering Conference; 2011 July 31–Aug 03; San Diego, CA. AIAA 2011-5981.

Osso JA et.al. Therapeutic radionuclide generators: 90Sr/90Y AND188W/188Re. Intl Atomic Energy Agency; 2009. Technical Reports series no.: 470.

Pelowitz DB, editor. MCNPX user's manual, version 2.7.0. Los Alamos (NM): Los Alamos National Laboratory; 2011 Apr. Report No.: LA-CP-11-00438.

Pustovalov AA, Gusev VV, Zaddé VV, Petrenko NS, Tsvetkov LA, Tikhomirov AV. 63Ni-based b-electric current source. Atomic Energy. 2007;103(6).

Reynolds SA. Theoretical and practical specific activities and other properties of common radionuclides. Oak Ridge (TN): Oak Ridge National Laboratory; 1973. Report No.: ORNL-TM-4167.

Russo J, Litz MS, William R II, Berk H, Cho H, Bigio DI, Weltz A, Alam TR. Planar and textured surface optimization for a tritium-based betavoltaic nuclear battery. Intl J Energy Research. 2019;43(9):4370–4389.

Spencer MG, Alam T. High power direct energy conversion by nuclear batteries. Appl Phys Rev. 2019;6:031305.

Surampudi R, Plichta E, Piszczor M et al. Energy storage technologies for future planetary science missions. Pasadena (CA): NASA Jet Propulsion Laboratory–Caltech; 2017 Dec. Report no.: JPL D-101146.

Theirrattanakul S, Prelas M. A methodology for efficiency optimization of betavoltaic cell design using an isotropic planar source having an energy dependent beta particle distribution, Applied Radiation and Isotopes. 2017;127:41–46.

Uhm YR, Choi BG, Kim JB, Jeong D-H, Son KJ. Study of a betavoltaic battery using electroplated nickel-63 on nickel foil as a power source. Nuclear Engineering and Technology. 2016;48:773–777.

Wu K, Dai C, Guo H. A theoretical study on silicon betavoltaics using Ni-63. Proceedings of the 2011 6th IEEE International Conference on Nano/Micro Engineered and Molecular Systems; 2011 Feb 20–23, Kaohsiung, Taiwan.

Weaver J, Burks SR, Liu KJ, Kao JPY, Rosen GM. In vivo EPR oximetry using an isotopically-substituted nitroxide: potential for quantitative measurement of tissue oxygen. Journal of Magnetic Resonance. 2016;271:68–74.

Wort, CJH, Balmer RS. Diamond as an electronic material. Materials Today. 2008;11(1–2).

Appendix A. Radioisotope Layer Thickness for 90% Saturable Energy Transfer

The energy transferred into the energy converter (EC) from the radioisotope (RI) layer is limited by self-shielding of the RI layer. The RI layer thickness that achieves 90% of saturable energy transferred is defined here to be an optimal RI layer thickness. This method has been described in Section 2 of this report.

The most efficient operation of a betavoltaic would be when as much as 50% of the energy stored in the isotope layer is delivered to the EC underneath the RI layer. Highest efficiency would typically be achieved by using the thinnest layer of RI deposited on the surface of the EC before self-shielding takes place. The efficiency (energy deposited in EC divided by energy released in RI layer) is plotted in red in Figs. C-1 through C-5 and the axis is on the left side of the figures. The most efficient 50% thin RI layer does not lend itself to maximizing power output.

In the following graphical results, three characteristics are plotted. The energy (per sec) contained within the RI layer (gray), the energy (per sec) deposited in the EC (yellow), and the ratio of energy deposited into the EC divided by the energy stored in the isotope layer (red). As the RI layer thickness increases, the energy stored within the RI layer continues to increase. However, the energy transferred to the EC is limited by RI self-shielding. When 90% of maximum transferrable energy is transferred, an optimized value for RI layer thickness is documented. From this RI layer thickness, the power transferred, and the activity required to maximize electrical output can be calculated.

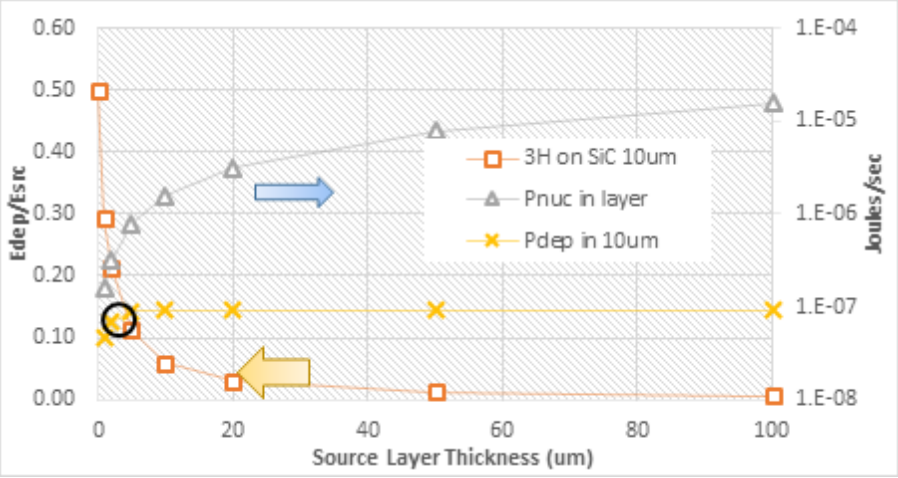

Fig. A-1 The RI thickness layer of ^{3}H at which 90% of maximum energy achievable is circled

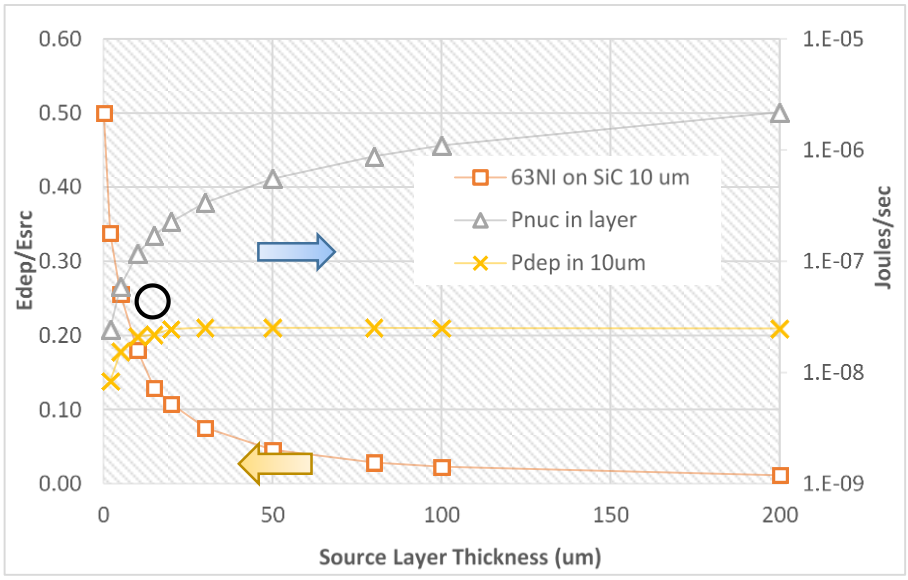

Fig. A-2 The RI thickness layer of ^{63}Ni at which 90% of maximum energy achievable is circled

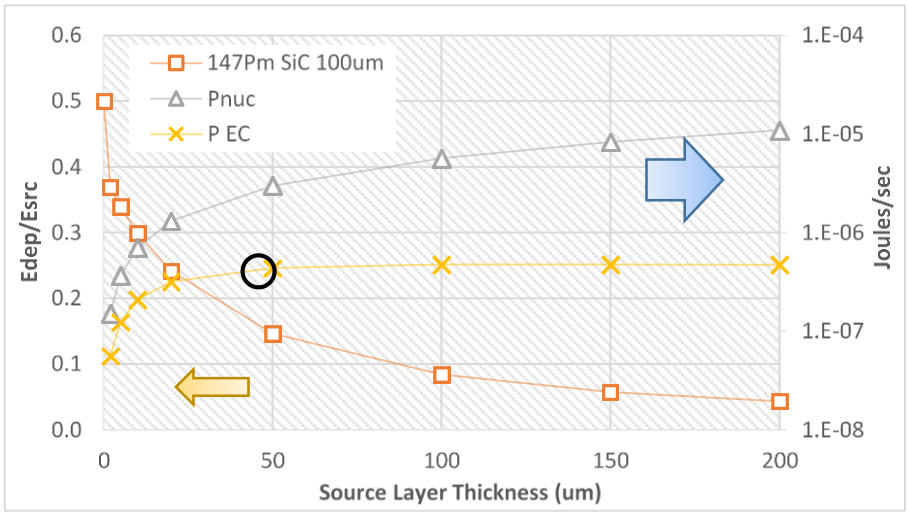

Fig. A-3 The RI thickness layer of ^{147}Pm at which 90% of maximum energy achievable is circled

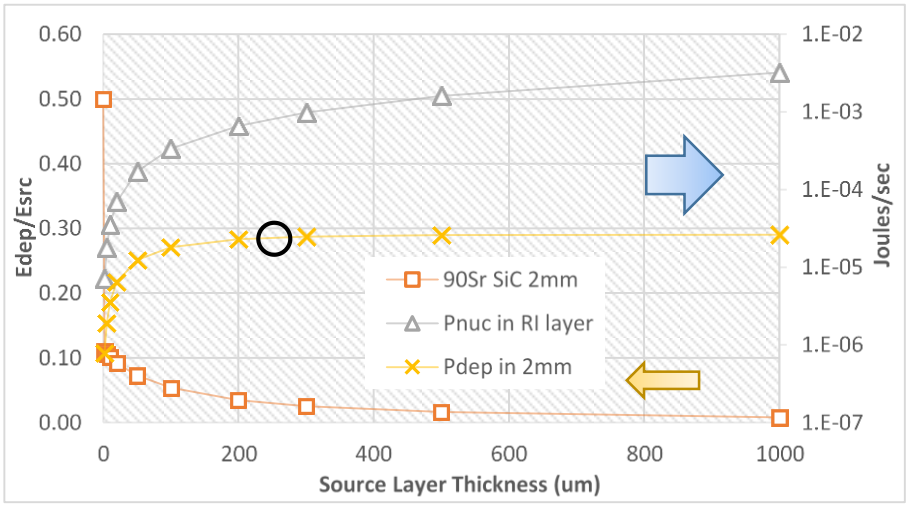

Fig. A-4 The RI thickness layer of ^{90}Sr at which 90% of maximum energy achievable is circled

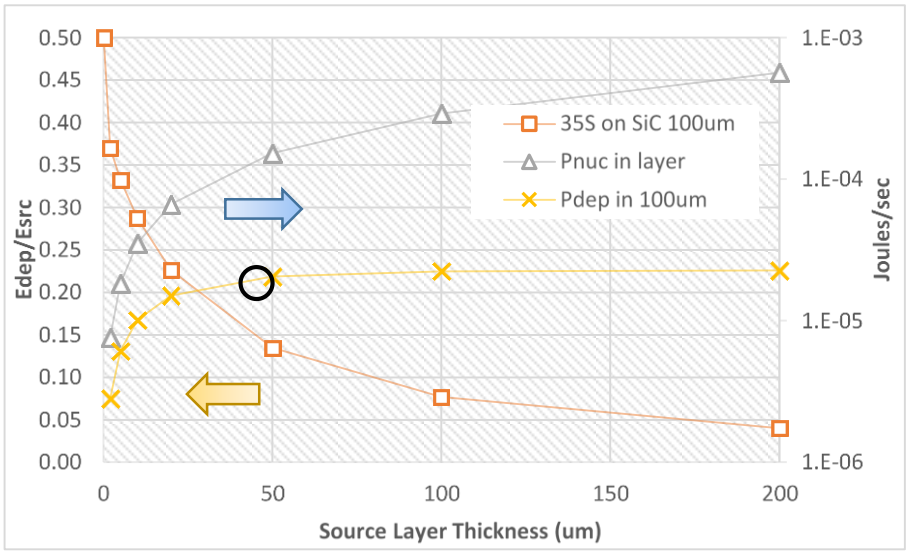

Fig. A-5 The RI thickness layer of ^{35}S at which 90% of maximum energy achievable is circled

The higher energy beta-emitting isotopes, ^{90}Sr for example, have a longer range before self-shielding within RI layer limits' effective surface activity on EC. The RI layer thicknesses for the most efficient operation of betavoltaic devices are all less than 5-µm thick RI layers. The efficiencies for ^{3}H, ^{63}Ni, ^{147}Pm, and ^{90}Sr are 29, 22, 7, and 0.5%, respectively.

Appendix B. Energy Converter Material Properties

A figure of merit (FOM) that can be used to look for wide-bandgap (WBG) semiconductors (SCs) for use in the future with higher energy radioisotope (RI) beta-emitters, and possible alpha emitters, are those compound SCs with small lattice constants and large bandgaps (BGs), among other characteristics.

$$FOM \quad \alpha \quad \frac{band\ gap}{lattice\ constant}$$

The FOM shown in Fig. B-1 compares the BG divided by the lattice constant (LC), as defined in the equation above. Aluminum nitride (AlN) is added to this chart only from the point of view of theoretical best, because no p-dopant is known for this compound making it difficult, at this time, to implement as a P-I-N device.

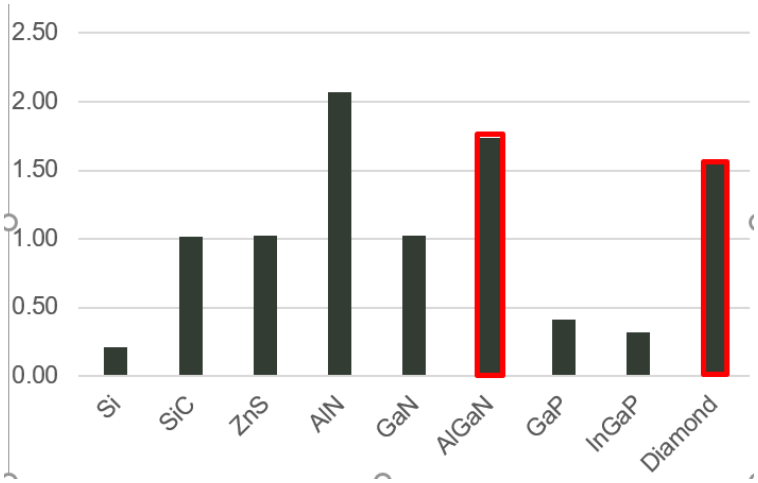

Fig. B-1 WBG SCs that show promise for use with high-energy betas and alphas are those that have high radiation tolerance FOMs

The values for BG and LCs are plotted in Fig. B-2. SC compounds with large BG and small LC have radiation tolerant characteristics when irradiated. Also identified in Fig. B-2 is the characteristic of direct versus indirect BG. In an indirect BG compound, a phonon is required for the transition of valence to conduction band, in order to accommodate the change in momentum. The phonon (lattice vibration) can make the process less efficient, but does have the consequence of slower recombination and therefore longer diffusion lengths, beneficial in a BV EC.

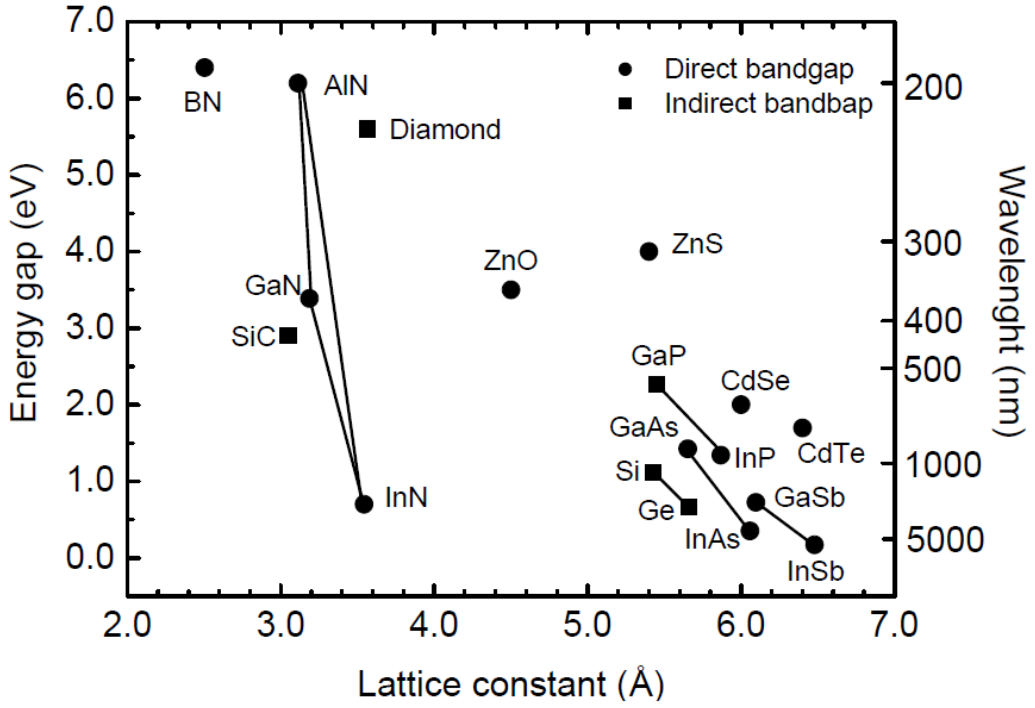

Fig. B-2 BGs and LCs of common SCs. Data from www.ioffe.rssi.ru.

The characteristics of several WBG SCs are tabulated in Table A-1. The BG, listed in units of eV, is proportional to the energy required to remove the electron from the atom. The displacement energy (E_{disp}), listed in units of eV, is proportional to the removal of the atom from the molecule. The LC, listed in units of angstroms, is proportional to the bond strength of the compound.

Table B-1 WBG SC characteristics

	ρ(g/cc)	BG(eV)	E_{disp} (eV)	LC(A°)
Si	2.32	1.14	12.9	5.42
SiC	3.21	3.23	38	3.18
ZnS	4.09	3.91	15	3.82
AlN	3.26	6.42	20	3.1
GaN	6.15	3.39	39	3.3
AlGaN	5.7	5.5	15	3.17
GaP	4.1	2.26	…	5.45
InGaP	4.47	1.79	4	5.65
Diamond	3.51	5.5	35	3.57

Note: GaP = gallium phosphide, InGaP = indium gallium phosphide.

Knock-on electrons are emitted from atoms by the passage of charged particles through matter. It is not surprising that the largest number of knock-on electrons is created by the ^{90}Sr betas because they have a much higher energy in comparison to the other isotopes in Fig. A-3a. A comparison of knock-on electron creation in WBG SC materials is shown in Fig. A-3b, where ^{63}Ni emitters generate the largest number of knock-on electrons in GaP.

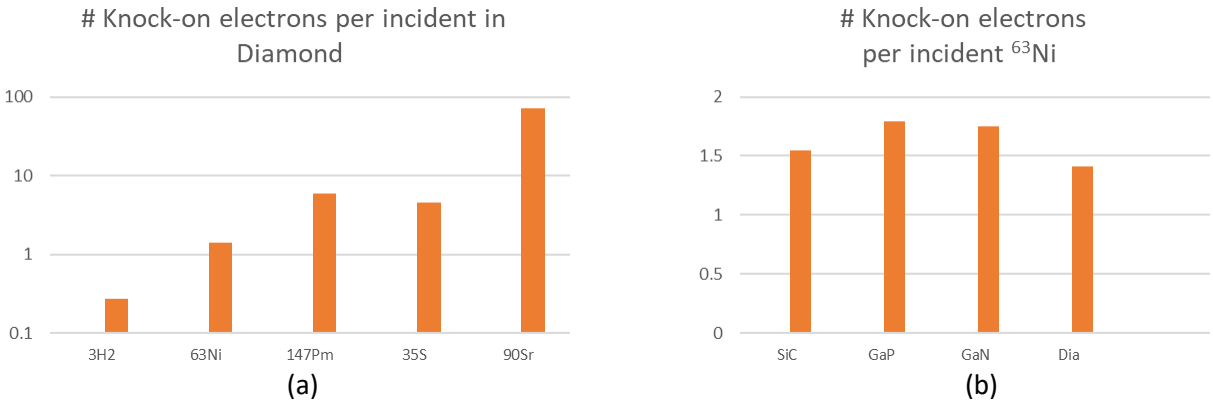

Fig. B-3 Creation of knock-on electrons is calculated with the Monte Carlo neutron-particle extended output data

While knock-on electrons are created most often in the WBG SCs described previously, there are four other physical phenomena that can create free electrons in the materials. The photoelectric (PE) describes an incident photon interacting with the atom such that the energy is absorbed and an orbital electron is emitted. The resulting vacancy results in the emission of characteristic X-rays of Auger electrons. The cross section for PE is approximately $Z^n/E^{3.5}$, where n varies between4–5 depending on X-ray energy

Auger electron emission occurs when a core electron is removed, from incident photon or electron. A vacancy is created in low orbital. An electron from a higher energy level may fall into the vacancy, resulting in a release of energy. Although most often this energy is released in the form of an emitted photon, the energy can also be transferred to another electron, which is ejected from the atom.

Compton recoil electrons are generated when part of the energy of a photon is transferred to an electron that recoils from the much higher energy photon.

Pair production occurs when a photon with sufficient energy (over 1 MeV) creates an electron–positron pair near a nucleus.

Appendix C. Energy Deposition Range in Energy Converter Materials

The energy deposition in a liquid medium containing isotopes has been modeled for five isotopes of interest and several wide-bandgap (WBG) semiconductors (SCs) of interest. The results are shown here for reasons of completeness, even though a table of values showing the distance in which 90% of the maximum saturable energy in the WBG SCs is tabulated in Section 3.2 (reproduced as Table B-1). The values for AlGaN are similar to that of GaN. The depth value for ^{147}Pm in SiC has been experimentally verified.

Table C-1 The thickness in EC within which 90% of the energy deposited by isotope is located

	SiC	**GaN**	**Diamond**	**ZnS**	**^{3}H-urea**	**$^{63}NiCl_2$**	**$^{147}PmCl_3$**	**$^{35}S(NH_4)_2$**	**$^{90}Sr(NOH_3)$**
^{3}H	0.62	0.23	0.42	1.4	3.4	...	...	...	...
^{63}Ni	4.4	2.2	3.3	8	...	11.5		...	...
^{147}Pm	28.4	14.8	23	40	...	...	42	...	...
^{35}S	18.5	10	15	36	...	...	...	45	...
^{90}Sr	149	130	69.5	231	...	...	...	...	198

The penetration depths for isotopes with energy content greater than 200 keV will penetrate the SC beyond the junction regions. The electron hole pairs created along the scattering path can still be collected into the junction region if the diffusion length of the SCs is compatible with the penetration depth. For example, the diffusion length of the indirect bandgap material SiC is approximately 100 µm, enabling charge collection for 68% of 90 Sr. The challenge then will be for the SiC to withstand the higher energy beta degradation because of damage to the crystal structure.

In the following graphical results of Figs. C-1, C-2, C-3, and C-4, the starting point for energy converting material is 2 µm. When finding the depth for 90% energy deposition, 2 µm must be subtracted.

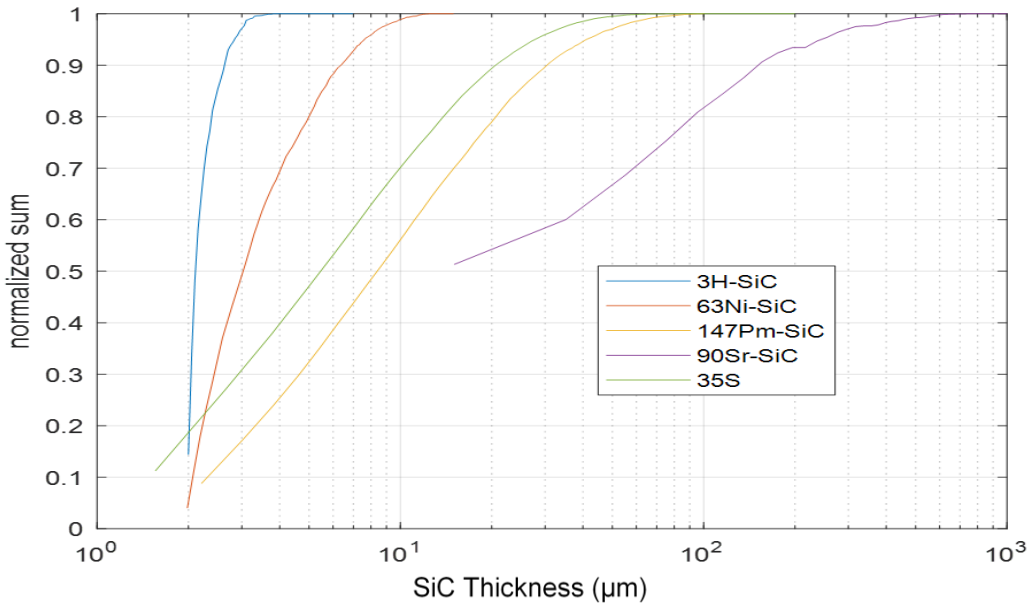

Fig. C-1 The normalized energy deposition in SiC is plotted as a function of depth in the material

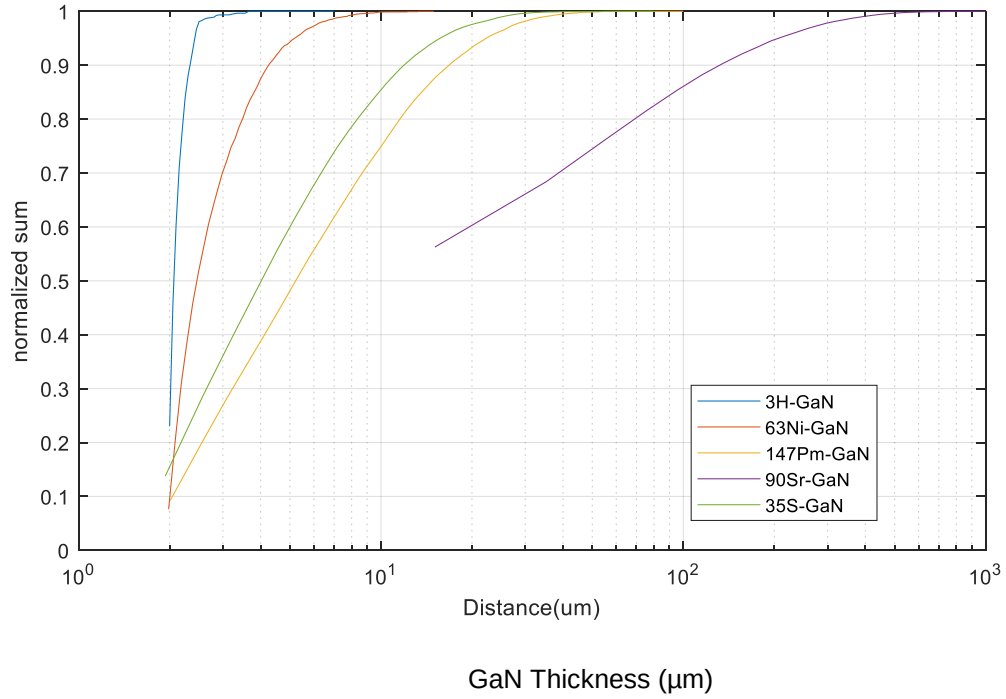

Fig. C-2 The normalized energy deposition in GaN is plotted as a function of depth in the material

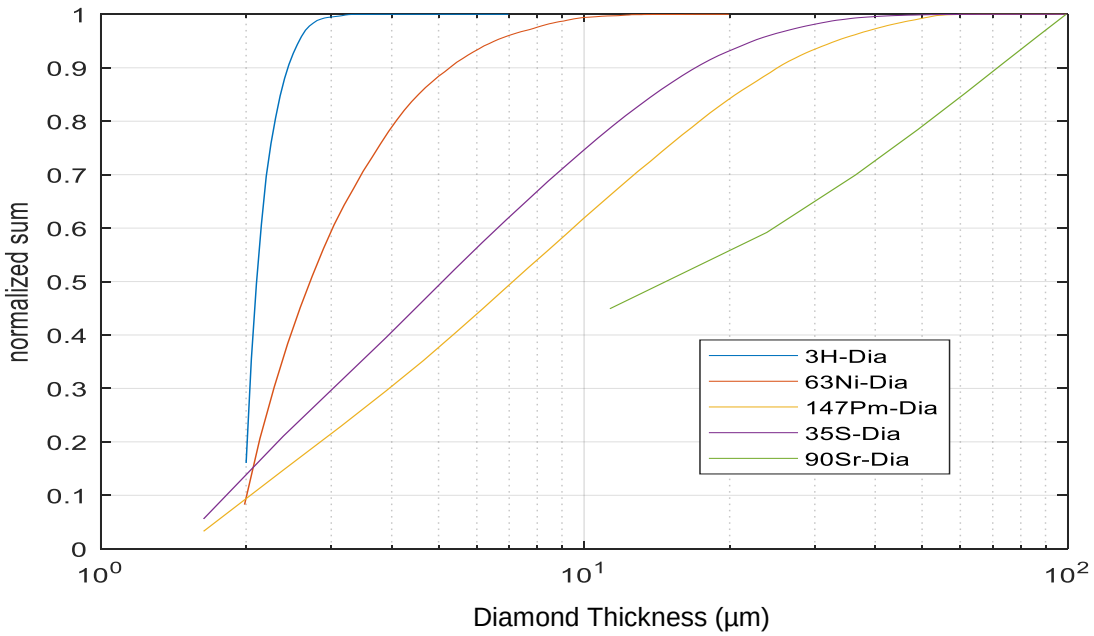

Fig. C-3 The normalized energy deposition in diamond is plotted as a function of depth

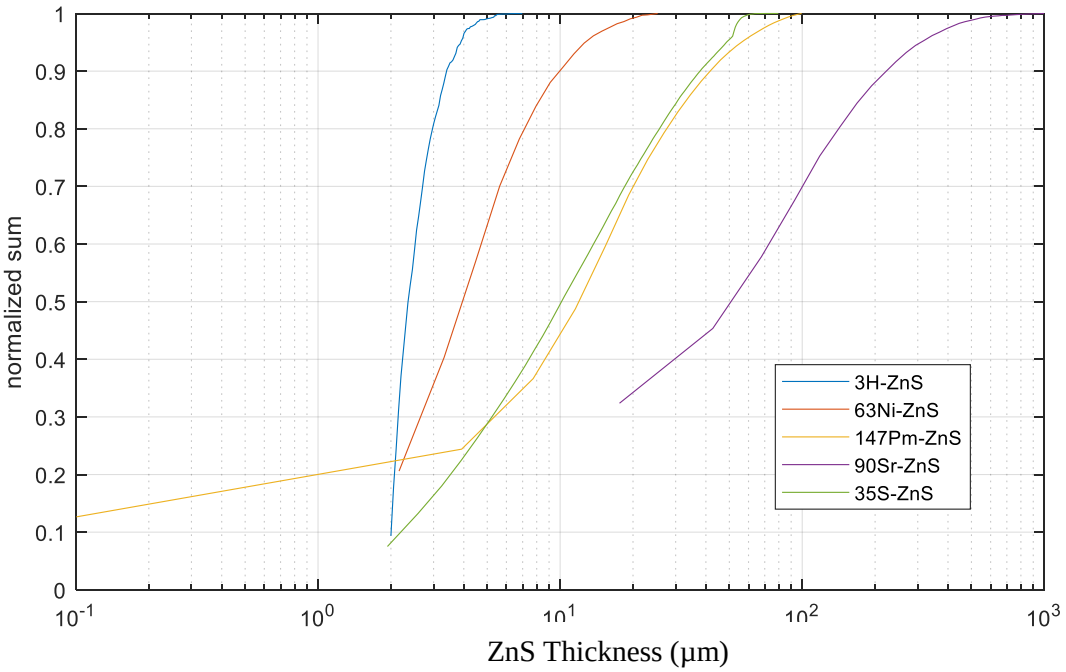

Fig. C-4 The normalized energy deposition in ZnS is plotted as a function of depth

List of Symbols, Abbreviations, and Acronyms

3-D	three-dimensional
AlGaN	aluminum gallium nitride
AlN	aluminum nitride
BG	bandgap
BV	betavoltaic
Cl	chlorine
EC	energy converter
ED	electro-deposition
GaN	gallium nitride
GaP	gallium phosphide
H	hydrogen
HFIR	High Flux Isotope Reactor
InGaP	indium gallium phosphide
LC	lattice constant
MCNPX	Monte Carlo neutron-particle extended
Ni	nickel
PE	photoelectric
Pm	promethium
RI	radioisotopes
SC	semiconductor
S	sulfur
Si	silicon
SiC	silicon carbide
Sr	strontium
WBG	wide-bandgap

Y	yttrium
ZnS	zinc sulfide

1 (PDF)	DEFENSE TECHNICAL INFORMATION CTR DTIC OCA
1 (PDF)	CCDC ARL FCDD RLD CL TECH LIB
1 (PDF)	CCDC ARL FCDD RLS CC M LITZ